A Potential-Based Integral Equation Method for Low-Frequency Electromagnetic Problems

Qin S. Liu, *Member, IEEE*, Sheng Sun, *Senior Member, IEEE*, and Weng Cho Chew, *Fellow, IEEE*

***Abstract*— In this paper, we propose a potential-based integral equation solver for low-frequency electromagnetic (EM) problems. In this formulation, the scalar potential (Φ) equation is solved in tandem with the vector potential (A) equation. The resulting system is immune to low-frequency catastrophe and accurate in capturing the electrostatic and magnetostatic physics. The fast convergence of the new A-Φ system, which is a typical symmetric saddle point problem, is made possible through the design of an appropriate left constraint preconditioner. Numerical examples validate the efficiency and stability of the novel formulation in solving both EM scattering and circuit problems over a wide frequency range up to very low frequencies.**

***Index Terms*— Circuit problems, integral equation, low-frequency catastrophe, scalar potential, scattering problems, vector potential.**

I. Introduction

MAXWELL'S equations formulated with **E**, **H**, **D**, and **B** are widely accepted for the electromagnetic (EM) physics from atomic length scale to galaxy length scale. Inspired by the increasing development in quantum optics, a wideband EM solution is desired from quantum physics regime to classical physics regime. However, computational EM methods deriving from Maxwell's equations, such as the electric-field integral equation (EFIE) methods, are usually susceptible to low-frequency catastrophe [1] and ill-conditioning with dense discretization [2]. This is exactly the difficulty in solving problems with small-size objects.

Various remedies to the low-frequency catastrophe of integral equations in EM problem have been well addressed in the literature. The loop-tree/loop-star method has been popularized by doing a quasi-Helmholtz decomposition to separate the vector and scalar potential parts [3]–[5]. The Calderón preconditioned EFIE (CP-EFIE) preconditions itself to obtain a well-conditioned second-kind operator with a bounded spectrum [6]–[10]. Stabilized CP-EFIE formulations with the loop-star decomposition are proposed at low frequencies [11]–[13]. And as an extension, the low-frequency nullspaces in multiconnected structures using the CP-EFIE are well studied in [14] and [15]. Another EFIE low-frequency breakdown remedy [16] transforms the EFIE into a generalized eigenvalue problem, and an accurate eigenmodal superposition of the current can be achieved after manually setting the small eigenvalues to be zero.

In the literature, the idea of potential separation by considering the current and charge as unknowns has been investigated for a stable formulation at low frequencies. The current and charge integral equation (CCIE), which includes the charge as extra unknowns in the combined field integral equation, is a well-conditioned second-kind integral equation for scattering problems with smooth closed objects [17]. Also, the partial element equivalent circuit (PEEC) is applied to the EFIE to obtain a separated potential integral equation [18]. Similar to the CCIE, the PEEC method uses the current and charge basis functions to separate the vector and scalar potentials. With the incorporation of conductor resistive loss and material dielectric loss, the system matrix is well behaved throughout a wide frequency range. Alternatively, the augmented EFIE (A-EFIE) is also a way to avoid the imbalance inherent in the EFIE by separating the vector and scalar potential terms [19]. The A-EFIE achieves low-frequency stability without searching for loop-tree/loop-star basis and can be easily integrated into the existing method of moments (MoM) solvers. Also, it inherits the capability of the standard EFIE without the limitation of basis type [20]–[22].

Note that in quantum physics, the formulations are better described using the vector potential **A** and scalar potential Φ, especially when the fields are zero and the potentials are nonzero [23]. Thus, to better bridge the EM regime and quantum regime, one can define the EM equations in the form of potentials. Most of the related works done in the literature are dealing with differential equations [24]–[28], which are usually immune to low-frequency catastrophe from which Maxwell's equations suffer. In [29], an integral equation system is constructed with the potentials as the unknowns to solve dielectric scattering problems at middle frequencies.

Manuscript received October 20, 2016; revised June 24, 2017; accepted August 10, 2017. Date of publication January 17, 2018; date of current version March 1, 2018. This work was supported in part by the National Natural Science Foundation of China under Grant 61622106, Grant 61721001, and Grant 61425010, in part by the Research Grants Council of Hong Kong under Grant GRF 17207114, in part by the University Grants Council of Hong Kong under Contract AoE/P-04/08. The work of W. C. Chew was supported in part by NSF ECCS under Grant 1609195 and in part by ANSYS Inc. under Grant PO37497. *(Corresponding author: Sheng Sun.)*

Q. S. Liu is with the Department of Electrical and Electronic Engineering, The University of Hong Kong, Hong Kong.

S. Sun is with the School of Electronic Engineering, University of Electronic Science and Technology of China, Chengdu 611731, China (e-mail: sunsheng@ieee.org).

W. C. Chew was with the University of Illinois at Urbana–Champaign, Champaign, IL 61801 USA. He is now with the Department of Electrical and Computer Engineering, Purdue University, West Lafayette, IN 47907 USA.

Color versions of one or more of the figures in this paper are available online at http://ieeexplore.ieee.org.

Digital Object Identifier 10.1109/TAP.2018.2794388

Recently, the decoupled potential integral equation was presented for scattering problems by solving the boundary value problems [30]. The potential-based integral equations have shown promise for a stabilized system for a wide frequency regime. Also, in [31] and [32], a vector potential integral equation is derived and implemented through the generalized Green's theorem and equivalence principle, where the current and normal component $\hat{n} \cdot \mathbf{A}$ (contribution of charge) are considered as unknowns. To match the additional number of unknowns, two equations are formulated from the tangential and normal directions, respectively.

In this paper, the scalar potential formulation is proposed and solved in tandem with the vector potential formulation at low frequencies to capture the correct physics, since the vector potential equation describes the magnetostatic world, while the scalar potential equation controls the electrostatic world. The new formulations are first presented in [33]. Here, we will show the detailed understanding, derivation, as well as the systematic spectrum analysis. The equation from the scalar potential Φ is derived with Lorenz's gauge. Combining with the vector potential formulation, the resultant system becomes symmetric. With the left constraint preconditioning based on a symmetric saddle point problem, the new system achieves excellent convergence for iterative solvers. It is verified in this paper that the new $\mathbf{A}$-Φ formulation is immune to low-frequency catastrophe and achieves stable conditioning properties when the mesh discretization becomes denser. Numerical results show that the new system works at a wide range of frequency for both scattering and circuit problems. The fact that the only integral kernel in the $\mathbf{A}$-Φ formulation is the scalar Green's function ensures the easy integration of the fast multipole algorithms (FMAs) based on existing techniques. Then, naturally the proposed method can be easily adapted to large-scale computations.

This paper is organized as follows. Section II introduces some preliminaries of this paper and the formulation for scalar potential is derived, which is solved in tandem with the vector potential formulation. In Section III, we discuss the recovery of conventional integral equations from the $\mathbf{A}$-Φ formulation. In Section IV, the equations are discretized and implemented using the MoM. The spectrum and conditioning analyses under different cases are discussed in this section. Also in Section V, the incident potentials for different cases are introduced. The large-scale computation issue is presented in Section VI. Numerical results are shown in Section VII for scattering problems, electrostatic problem, magnetostatic problem, and large-scale computation. Then, this paper ends with Section VIII for conclusion.

II. Formulations

From Maxwell's equations, the vector potential $\mathbf{A}$ and scalar potential Φ are defined as

$$\mathbf{B} = \nabla \times \mathbf{A} \tag{1}$$

$$\mathbf{E} = i\omega\mathbf{A} - \nabla\Phi. \tag{2}$$

Based on the constitutive relations $\mathbf{D} = \epsilon\mathbf{E}, \mathbf{B} = \mu\mathbf{H}$, and the Lorenz gauge $\nabla \cdot \mathbf{A} = i\omega\mu\epsilon\Phi$, the vector and scalar potential equations are decoupled from each other [34]

$$\nabla^2\mathbf{A} + k^2\mathbf{A} = -\mu\mathbf{J} \tag{3}$$

$$\nabla^2\Phi + k^2\Phi = -\rho/\epsilon \tag{4}$$

where k is the wavenumber, ϵ and μ are the permittivity and permeability, respectively, and $\mathbf{J}$ and ρ are the current and charge sources in the solvable region.

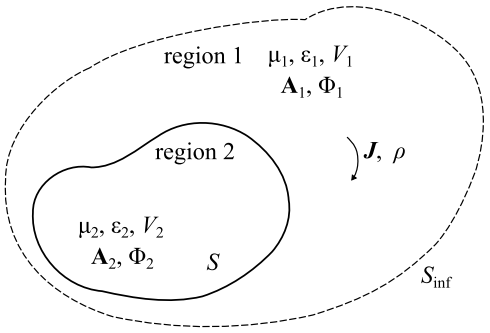

Fig. 1. Configuration of media and regions used to derive the scalar potential equation.

For a problem with two regions, as shown in Fig. 1, the sources in region 1 are the current density $\mathbf{J}$ and the produced charge density ρ. We consider region 2 to be a PEC scatterer and region 1 to be the free space; then, based on (3), the equivalence principle and extinction theorem for vector potential integral equation with scalar Green's function can be derived as [31]

$$\left.\begin{array}{l}\mathbf{r} \in V_1,\ \mathbf{A}_1(\mathbf{r}) \\ \mathbf{r} \in V_2,\ 0\end{array}\right\} = \mathbf{A}_{\text{inc}}(\mathbf{r}) + \int_S dS'\{\mu_1 g_1(\mathbf{r},\mathbf{r}')\mathbf{J}_1(\mathbf{r}') + \hat{n}' \cdot \mathbf{A}_1(\mathbf{r}')\nabla' g_1(\mathbf{r},\mathbf{r}')\} \tag{5}$$

where $\mathbf{A}_{\text{inc}}$ is the incident vector potential. Here, μ_1 is the permeability and $\mathbf{A}_1(\mathbf{r})$ is the vector potential for field point $\mathbf{r}$ in region 1. Also, $\mathbf{J}_1$ is the equivalent current on the PEC surface, and $g_1(\mathbf{r},\mathbf{r}')$ is the free space scalar Green's function which is defined as

$$g_1(\mathbf{r},\mathbf{r}') = \frac{e^{ik_1|\mathbf{r}-\mathbf{r}'|}}{4\pi\ |\ \mathbf{r}-\mathbf{r}'\ |} \tag{6}$$

where $\mathbf{r}'$ is the source point location. Here, we denote the unknown $\hat{n}\cdot\mathbf{A}$ with Σ. By applying the extinction theorem on the surface S, the equation can be written as

$$0 = \mathbf{A}_{\text{inc}}(\mathbf{r}) + \int_S dS'\{\mu_1 g_1(\mathbf{r},\mathbf{r}')\mathbf{J}_1(\mathbf{r}') + \nabla' g_1(\mathbf{r},\mathbf{r}')\Sigma_1(\mathbf{r}')\},\ \mathbf{r} \in S^+. \tag{7}$$

The scalar potential formulation can be simply derived from the vector formulation (5) and the Lorenz gauge. The governing potentials for regions 1 and 2 satisfy the scalar wave equation (4), while in region 2, $\rho_2 = 0$. Green's function in region 1 can be defined as

$$(\nabla^2 + k_1^2)g_1(\mathbf{r},\mathbf{r}') = -\delta(\mathbf{r}-\mathbf{r}') \tag{8}$$

where (6) is a possible choice of solution satisfying the radiation condition.

Taking the divergence of (7) and incorporating the Lorenz gauge, it becomes

$$0 = i\omega\mu_1\epsilon_1\Phi_{\rm inc}(\mathbf{r}) + \int_S dS'\big\{\mu_1 g_1(\mathbf{r},\mathbf{r}')\nabla'\cdot\mathbf{J}_1(\mathbf{r}') + \nabla'^2 g_1(\mathbf{r},\mathbf{r}')\Sigma_1((\mathbf{r}'))\big\},\ \ \mathbf{r}\in S^+. \quad (9)$$

Using (8), and that $\mathbf{r}\neq\mathbf{r}'$, the scalar potential formulation for PEC surface can be obtained as

$$-i\omega\mu_1\epsilon_1\Phi_{\rm inc}(\mathbf{r}) = \int_S dS'\big\{\mu_1 g_1(\mathbf{r},\mathbf{r}')\nabla'\cdot\mathbf{J}_1(\mathbf{r}')+k_1^2 g_1(\mathbf{r},\mathbf{r}')\Sigma_1(\mathbf{r}')\big\},\ \mathbf{r}\in S^+. \quad (10)$$

It is important to notice that the physical meaning of (10), as shown in the following, is the weak form of the current continuity condition by using the scalar Green's theorem, which follows from the scalar wave equation (4).

By multiplying (4) by g_1 and (8) by Φ_1, subtracting the resultant equations, and then integrating over the volume V_1, the volume integral equation for scalar potential is obtained [35]. With the help of Gauss' theorem, the volume integral can be written in the form of surface integral as follows:

$$\Phi_1(\mathbf{r}') = \Phi_{\rm inc}(\mathbf{r}') - \int_{S+S_{\rm inf}} dS\hat{n}\cdot[g_1(\mathbf{r},\mathbf{r}')\nabla\Phi_1(\mathbf{r}) - \Phi_1(\mathbf{r})\nabla g_1(\mathbf{r},\mathbf{r}')],\ \ \mathbf{r}'\in V_1 \quad (11)$$

where $\Phi_{\rm inc}$ is the incident field generated by the charge source ρ in V_1

$$\Phi_{\rm inc}(\mathbf{r}') = \frac{1}{\epsilon}\int_{V_1} dV g_1(\mathbf{r},\mathbf{r}')\rho_1(\mathbf{r}). \quad (12)$$

Due to the radiation boundary condition, the integral over $S_{\rm inf}$ vanishes in (11). After swapping $\mathbf{r}$ and $\mathbf{r}'$, the equation for the whole space can be written as

$$\left.\begin{array}{l}\mathbf{r}\in V_1,\ \Phi_1(\mathbf{r})\\ \mathbf{r}\in V_2,\ 0\end{array}\right\} = \Phi_{\rm inc}(\mathbf{r}) - \int_S dS'\hat{n}'\cdot[g_1(\mathbf{r},\mathbf{r}')\nabla'\Phi_1(\mathbf{r}') - \Phi_1(\mathbf{r}')\nabla' g_1(\mathbf{r},\mathbf{r}')]. \quad (13)$$

In V_2, $\nabla\Phi_1(\mathbf{r})$ and $\Phi_1(\mathbf{r})$ actually act as the equivalent impressed surface sources. They generate a field in V_2 that exactly cancels with the incident field, which is the extinction theorem. The scalar Green's theorem (13), where $g(\mathbf{r},\mathbf{r}')$ and $\hat{n}\cdot\nabla g(\mathbf{r},\mathbf{r}')$ are the integral kernels, includes the unknowns for Φ and $\hat{n}\cdot\nabla\Phi$. According to (2), the surface charge density can be written as

$$\sigma = \hat{n}\cdot\epsilon\mathbf{E} = i\omega\epsilon(\hat{n}\cdot\mathbf{A}) - \hat{n}\cdot\epsilon\nabla\Phi \quad (14)$$

from which it shows that $\hat{n}\cdot\nabla\Phi$ is part of the contribution to the surface charge and the formerly defined $\Sigma = \hat{n}\cdot\mathbf{A}$ is actually the other part of contribution.

As a PEC boundary condition, $\Phi = 0$ on the surface. Thus, the surface equation of the scalar Green's theorem (13) can be reduced to

$$\Phi_{\rm inc}(\mathbf{r}) = \int_S dS'\hat{n}'\cdot[g_1(\mathbf{r},\mathbf{r}')\nabla'\Phi_1(\mathbf{r}')] \quad \mathbf{r}\in S^+. \quad (15)$$

Substituting (15) into (10) and considering the fact of (14), we can obtain

$$\int_S dS' g_1(\mathbf{r},\mathbf{r}')\{\nabla'\cdot\mathbf{J}(\mathbf{r}') - i\omega\sigma(\mathbf{r}')\} = 0. \quad (16)$$

This is a weak form of the current continuity condition with Green's function as the weighting kernel. It implies that the current continuity condition is implicitly imposed in the vector and scalar potential formulations through the Lorenz gauge. A similar conclusion with that in (16) can also been found in [36] and [37], where Green's function is manually applied as the integral kernel on the current continuity condition in the field-based formulations in order to improve the conditioning of the system.

III. Recovery of EFIE and MFIE Formulations

Based on (1) and (2), the conventional field-based integral equations can be derived from the potential-based integral equations. Similarly, taking the gradient of (15) together with (7), the EFIE can be obtained as

$$-\mathbf{E}_{\rm inc}(\mathbf{r}) = -i\omega\mathbf{A}_{\rm inc}(\mathbf{r}) + \nabla\Phi_{\rm inc}(\mathbf{r}) = i\omega\int_S dS'[\mu_1 g_1(\mathbf{r},\mathbf{r}')\mathbf{J}_1(\mathbf{r}') + \nabla' g_1(\mathbf{r},\mathbf{r}')\Sigma_1(\mathbf{r}')] - \nabla\int_S dS' g_1(\mathbf{r},\mathbf{r}')\hat{n}'\cdot\nabla'\Phi_1(\mathbf{r}'). \quad (17)$$

Note that the first term in (17) is the vector potential term in the original EFIE with the scalar Green's function. The second term and the third term can be deduced to be

$$i\omega\int_S dS'\nabla' g_1(\mathbf{r},\mathbf{r}')\Sigma_1(\mathbf{r}') - \nabla\int_S dS' g_1(\mathbf{r},\mathbf{r}')\hat{n}'\cdot\nabla'\Phi_1(\mathbf{r}') = -\int_S dS'\nabla g_1(\mathbf{r},\mathbf{r}')\frac{\sigma_1(\mathbf{r}')}{\epsilon} \quad (18)$$

which is the scalar potential term in the EFIE with σ_1 denoting the surface charge. It is interesting to notice that the vector potential formulation in fact contributes the EFIE vector potential term and one part of the scalar potential term, while the scalar potential formulation contributes to the other part of the EFIE scalar potential term. As ω approaching to zero, the only component in the electric field is from the scalar potential, which is the contribution from part of the surface charge.

On the other hand, the magnetic-field integral equation (MFIE) can be directly obtained from (7) by taking the curl of both sides of the equation. Considering the constitutive relation $\mathbf{B} = \mu\mathbf{H}$ and the fact that $\nabla\times\nabla g(\mathbf{r},\mathbf{r}') = 0$, it can be derived as

$$-\mathbf{H}_{\rm inc}(\mathbf{r}) = \nabla\times\int_S dS' g_1(\mathbf{r},\mathbf{r}')\mathbf{J}_1(\mathbf{r}') \quad (19)$$

which is just the well-known MFIE for the scalar Green's function.

IV. Discretization and Implementation

A. Formulation Discretization

Now, we have arrived at the $\mathbf{A}$-Φ formulation for a PEC object as (7) and (10). The excitations are the incident vector

potential and scalar potential, and the unknowns are the current $\mathbf{J}_1$ and the normal vector potential component Σ_1. By discretizing $\mathbf{J}_1$ with the RWG basis function $\mathbf{f}_n$ and Σ_1 with the pulse basis function h_n, and then testing (7) with the RWG function and (10) with the pulse function, the matrix representation of the **A**-Φ system can be written as

$$\begin{bmatrix} \mu_1\overline{\mathbf{\Gamma}}_{11} & \overline{\mathbf{\Gamma}}_{12} \\ \overline{\mathbf{\Gamma}}_{21} & \omega^2\epsilon_1\overline{\mathbf{\Gamma}}_{22} \end{bmatrix} \begin{bmatrix} \mathbf{j}_1 \\ \boldsymbol{\psi}_1 \end{bmatrix} = \begin{bmatrix} -\boldsymbol{\alpha}_{\text{inc}} \\ -i\omega\epsilon_1\boldsymbol{\phi}_{\text{inc}} \end{bmatrix} \tag{20}$$

where $\mathbf{j}_1$ and $\boldsymbol{\psi}_1$ denote the basis coefficients for $\mathbf{J}_1$ and Σ_1, respectively. The matrix elements are

$$\begin{aligned} [\overline{\mathbf{\Gamma}}_{11}]_{mn} &= \langle \mathbf{f}_m, g_1, \mathbf{f}_n \rangle, \quad [\overline{\mathbf{\Gamma}}_{12}]_{mn} = \langle \nabla \cdot \mathbf{f}_m, g_1, h_n \rangle \\ [\overline{\mathbf{\Gamma}}_{21}]_{mn} &= \langle h_m, g_1, \nabla \cdot \mathbf{f}_n \rangle, \quad [\overline{\mathbf{\Gamma}}_{22}]_{mn} = \langle h_m, g_1, h_n \rangle \end{aligned} \tag{21}$$

and the right-hand side vector elements are

$$[\boldsymbol{\alpha}_{\text{inc}}]_m = \langle \mathbf{f}_m, \mathbf{A}_{\text{inc}} \rangle, \quad [\boldsymbol{\phi}_{\text{inc}}]_m = \langle h_m, \Phi_{\text{inc}} \rangle. \tag{22}$$

Here, the second equation is divided by μ_1 in the matrix formulation, so that the matrix system presented in (20) becomes symmetric, since $[\overline{\mathbf{\Gamma}}_{12}]_{mn} = [\overline{\mathbf{\Gamma}}_{21}]_{\text{nm}}$. The notations $\boldsymbol{\alpha}_{\text{inc}}$ and ϕ_{inc} are the right-hand side excitation vector of $\mathbf{A}_{\text{inc}}$ and Φ_{inc} tested with the RWG function and pulse function, respectively. Furthermore, the inner product in the angle brackets is defined as

$$\langle \mathbf{f}(\mathbf{r}), \mathbf{h}(\mathbf{r}) \rangle = \int_S dS \mathbf{f}(\mathbf{r}) \cdot \mathbf{h}(\mathbf{r}) \tag{23}$$

$$\langle \mathbf{f}(\mathbf{r}), g_1(\mathbf{r}, \mathbf{r}'), \mathbf{h}(\mathbf{r}') \rangle = \int_S dS \mathbf{f}(\mathbf{r}) \cdot \int_S dS' g_1(\mathbf{r}, \mathbf{r}') \mathbf{h}(\mathbf{r}') \tag{24}$$

where $\mathbf{f}(\mathbf{r})$ and $\mathbf{h}(\mathbf{r})$ can be replaced by scalar functions.

Obviously, no frequency normalization is needed as what one does for loop-tree/loop-star method, since no frequency term outside the integral is involved except for the bottom-right block in the new **A**-Φ formulation after separating the vector and scalar potentials.

B. Coefficient Normalization

Observing the matrix in (20), the matrix elements $\overline{\mathbf{\Gamma}}_{ij}$ $(i, j = 1, 2)$ are of the same order. The existence of the coefficients μ_1, ϵ_1, and ω^2 causes imbalanced diagonal element values of the block matrix system (very small values in the top-left block and very large values in the bottom-right block), leading to the inefficient convergence when an iterative solver is involved. Considering region 1 to be free space, an appropriate coefficient normalization is applied in the system presented as follows:

$$\begin{bmatrix} \overline{\mathbf{\Gamma}}_{11} & \overline{\mathbf{\Gamma}}_{12} \\ \overline{\mathbf{\Gamma}}_{21} & k_0^2\overline{\mathbf{\Gamma}}_{22} \end{bmatrix} \begin{bmatrix} \mathbf{j}_1/c_0 \\ \boldsymbol{\psi}_1/\eta_0 \end{bmatrix} = \begin{bmatrix} -\boldsymbol{\alpha}_{\text{inc}}/\eta_0 \\ -ik_0\epsilon_1\boldsymbol{\phi}_{\text{inc}} \end{bmatrix} \tag{25}$$

where c_0, η_0, and k_0 are the light velocity, intrinsic impedance, and wavenumber in vacuum, respectively. Here, an example of the scattering of a unit PEC sphere at 10 MHz is used to present the coefficient normalization effect. The sphere is discretized into 867 edges and 578 patches. Fig. 2 shows the eigenvalue spectrums before and after coefficient normalization. Here, only the positive values are shown with logarithmic coordinates. Before the coefficient normalization,

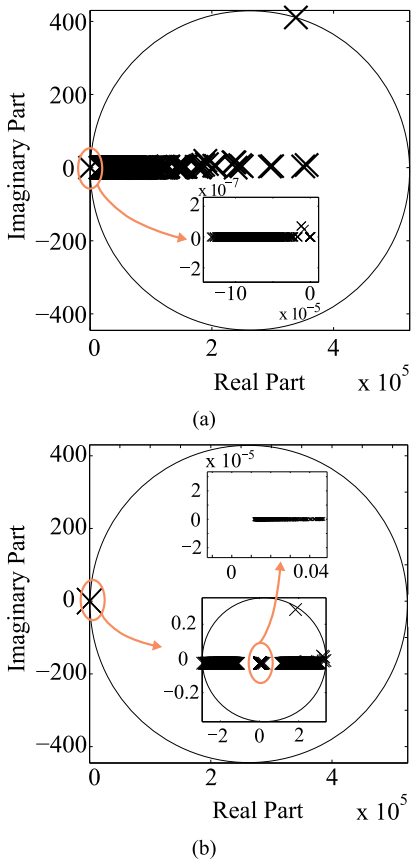

Fig. 2. Eigenvalue spectrum distribution of the **A**-Φ system. (a) Before coefficient normalization. (b) After coefficient normalization.

the eigenvalues are largely divergently distributed with some very small values accumulating around zero. Thus, the system is ill-conditioned. With the appropriate normalization, the spectrum is distributed within a small circle which is away from zero. Later, we will show that the normalized system can achieve stable convergence with a conventional iterative solver, such as the restarted generalized minimal residual (GMRES), especially for denser meshes.

The matrix system presented in (25) is still symmetric. Since the frequency factor locates only in the bottom-right block of the matrix, there will be no frequency imbalance issue that causes the low-frequency breakdown problem in the EFIE. Also, it is noted that (25) is actually a typical symmetric saddle point problem, where the top-left block is symmetric and the bottom-right block is approaching to zero at low frequencies. It is favorable for one to solve such a system for there are typical preconditioners in mathematics. The symmetry of the whole system enables the simplicity of the preconditioner and ensures the efficient convergence after preconditioning.

C. Left Constraint Preconditioning

As it has been well addressed in [38], the left constraint preconditioner $\overline{\mathcal{P}}_c^{-1}$ is applied here. Denote the block matrix in (25) as $\overline{\mathbf{\Gamma}}$, thus the preconditioned system matrix now can

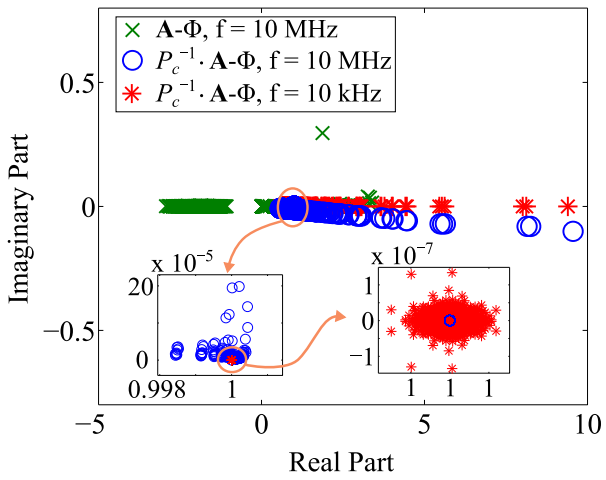

Fig. 3. Eigenvalue spectrum distribution of the preconditioned **A**-Φ system.

be written as $\overline{\mathcal{P}}_c^{-1} \cdot \overline{\mathbf{\Gamma}}$, where

$$\overline{\mathcal{P}}_c = \begin{bmatrix} \overline{\mathbf{G}} & \overline{\mathbf{\Gamma}}_{21}^T \\ \overline{\mathbf{\Gamma}}_{21} & k_0^2 \overline{\mathbf{\Gamma}}_{22} \end{bmatrix} \tag{26}$$

where $\overline{\mathbf{G}}$ is an approximation of $\overline{\mathbf{\Gamma}}_{11}$. For simplicity, $\overline{\mathbf{G}}$ is chosen as the diagonal of $\overline{\mathbf{\Gamma}}_{11}$ and $\overline{\mathbf{\Gamma}}_{21}^T = \overline{\mathbf{\Gamma}}_{12}$. The inverse of $\overline{\mathcal{P}}_c$ can be easily obtained through

$$\overline{\mathcal{P}}_c^{-1} = \begin{bmatrix} \overline{\mathbf{I}} & -\overline{\mathbf{G}}^{-1}\overline{\mathbf{\Gamma}}_{21}^T \\ O & \overline{\mathbf{I}} \end{bmatrix} \cdot \begin{bmatrix} \overline{\mathbf{G}}^{-1} & O \\ O & \overline{\mathbf{S}}^{-1} \end{bmatrix} \cdot \begin{bmatrix} \overline{\mathbf{I}} & O \\ -\overline{\mathbf{\Gamma}}_{21}\overline{\mathbf{G}}^{-1} & \overline{\mathbf{I}} \end{bmatrix} \tag{27}$$

where $\overline{\mathbf{S}} = -(-k_0^2 \overline{\Gamma}_{22} + \overline{\mathbf{\Gamma}}_{21}\overline{\mathbf{G}}^{-1}\overline{\mathbf{\Gamma}}_{21}^T)$ is the Schur complement of $\overline{\mathbf{\Gamma}}$. The procedure is not expensive at all even when $\overline{\mathbf{S}}$ is completely dense. Techniques, such as approximate and sparse factorization methods [38], can be used to efficiently and approximately form and invert $\overline{\mathbf{S}}$. Later, it will be shown in Section VI that a simple diagonal manner of the matrices forming the Schur complement can be chosen for large-scale computations. The preconditioner is specially efficient, while the frequency is approaching zero and the bottom-right block in (26) becomes zero.

The impedance matrices with and without the left constraint preconditioner are built based on the same PEC sphere example, as illustrated in Section IV-B. The eigenvalue spectrum of the matrices is shown in Fig. 3. After preconditioning, the system becomes quasi-positive definite. And the eigenvalues are almost real, since their imaginary parts are much smaller than the real parts, which is more obvious as frequency becomes lower. For a typical symmetric saddle point problem, the matrix elements are assumed to be real, and the solved eigenvalues are real accordingly. We can quasi-equivalently apply the spectrum theory of the saddle point problem on the preconditioned **A**-Φ formulation at low frequencies. Theoretically, when with zero bottom-right block, after constraint preconditioning, the eigenvalue 1 is with the multiplicity of $2m$, where m is the row dimension of the matrix $\overline{\mathbf{\Gamma}}_{21}$ [39]. And obviously, the better $\overline{\mathbf{G}}$ approximates $\overline{\mathbf{\Gamma}}_{11}$, the more the eigenvalues clustering around 1. Here, the matrix $\overline{\mathbf{G}}$ is chosen to be the diagonal of $\overline{\mathbf{\Gamma}}_{11}$. A number of eigenvalues are shown to accumulate around 1 in the zoomed-in figures in Fig. 3. As k goes to zero, the bottom-right block of the original matrix goes to zero. In the sphere example

$$\overline{\mathbf{\Gamma}}_{21} \in \mathbb{C}^{578\times 867} \Rightarrow 2\ m = 1156. \tag{28}$$

At the frequency of 10 MHz, there are 1152 eigenvalues clustered around 1 within an error of 1%, while at 10 kHz, the number is 1155 within a very small error of 10^{-6}. It implies that the diagonal approximation of $\overline{\mathbf{G}}$ is appropriate for an efficient preconditioning, especially at low frequencies. Furthermore, the last m eigenvectors corresponding to eigenvalues 1 is of the form $[\mathbf{0}, \mathbf{y}]^T$, which is a pure eigenbasis for the charge contribution.

D. Conditioning With Dense Mesh Discretization

Further spectrum analysis on the preconditioned **A**-Φ formulation system can be applied to discuss the conditioning of the system if the mesh density becomes higher where the EFIE formulation also breaks down.

Theoretically, referring to the theory in [38] and [42], for a preconditioned symmetric saddle point matrix $\overline{\mathcal{P}}_c^{-1} \cdot \overline{\mathbf{\Gamma}}$, where $\overline{\mathcal{P}}_c$ is given by (26) (here $\overline{\mathbf{G}}$ is the symmetric and positive definite by being chosen as the diagonal of $\overline{\mathbf{\Gamma}}_{11}$), the eigenvalues are of the form

$$\lambda = \gamma + 1 \tag{29}$$

where γ is defined by the generalized eigenvalue problem

$$\gamma \begin{bmatrix} \overline{\mathbf{I}} & \overline{\mathbf{B}}^T \\ \overline{\mathbf{B}} & k_0^2 \overline{\mathbf{\Gamma}}_{22} \end{bmatrix} \begin{bmatrix} \tilde{\mathbf{u}} \\ \mathbf{v} \end{bmatrix} = \begin{bmatrix} \overline{\mathbf{E}} & 0 \\ 0 & 0 \end{bmatrix} \begin{bmatrix} \tilde{\mathbf{u}} \\ \mathbf{v} \end{bmatrix} \tag{30}$$

where $\overline{\mathbf{B}} = \overline{\mathbf{\Gamma}}_{21}\overline{\mathbf{G}}^{-(1/2)}$, $\overline{\mathbf{E}} = \overline{\mathbf{G}}^{-(1/2)}\overline{\mathbf{\Gamma}}_{11}\overline{\mathbf{G}}^{-(1/2)} - \overline{\mathbf{I}}$, and $\tilde{\mathbf{u}} = \overline{\mathbf{G}}^{(1/2)}\mathbf{u}$. Apparently, the above-mentioned generalized eigenvalue problem has at least m zero eigenvalues. It is validated that the generalized eigenvalue problem in (30) has a zero eigenvalue solution with the multiplicity of $m+q$, where q is the dimension of the nullspace of $\overline{\mathbf{E}}$. This conclusion is easy to arrive at due to the fact that $\gamma = 0$ if and only if $\overline{\mathbf{E}}\tilde{\mathbf{u}} = 0$ and $\tilde{\mathbf{u}} \neq 0$.

When $\gamma \neq 0$, here we assume that the matrix $\overline{\mathbf{\Gamma}}_{22}$ is invertible, the nonzero eigenvalues can be obtained from the top equation in (30) as

$$\gamma = \frac{\tilde{\mathbf{u}}^*\overline{\mathbf{E}}\tilde{\mathbf{u}}}{\tilde{\mathbf{u}}^*\tilde{\mathbf{u}} + \tilde{\mathbf{u}}^*\overline{\mathbf{B}}^T\mathbf{v}}. \tag{31}$$

What can be obtained from the bottom equation in (30) is that

$$\gamma\,\overline{\mathbf{B}}\tilde{\mathbf{u}} = -\gamma\, k_0^2 \overline{\mathbf{\Gamma}}_{22}\mathbf{v}. \tag{32}$$

Hence, since $[\tilde{\mathbf{u}} \quad \mathbf{v}]^T$ is the normalized eigenvector, the elements of the term $\tilde{\mathbf{u}}^*\overline{\mathbf{B}}^T$ in (31) should be of very small values at low frequencies due to the existence of k_0^2 factor in (32). Thus, it can be deduced that

$$|\gamma| \approx \left| \frac{\tilde{\mathbf{u}}^*\overline{\mathbf{E}}\tilde{\mathbf{u}}}{\tilde{\mathbf{u}}^*\tilde{\mathbf{u}}} \right| \leq \frac{\|\tilde{\mathbf{u}}^*\|\|\overline{\mathbf{E}}\|\|\tilde{\mathbf{u}}\|}{|\tilde{\mathbf{u}}^*\tilde{\mathbf{u}}|}. \tag{33}$$

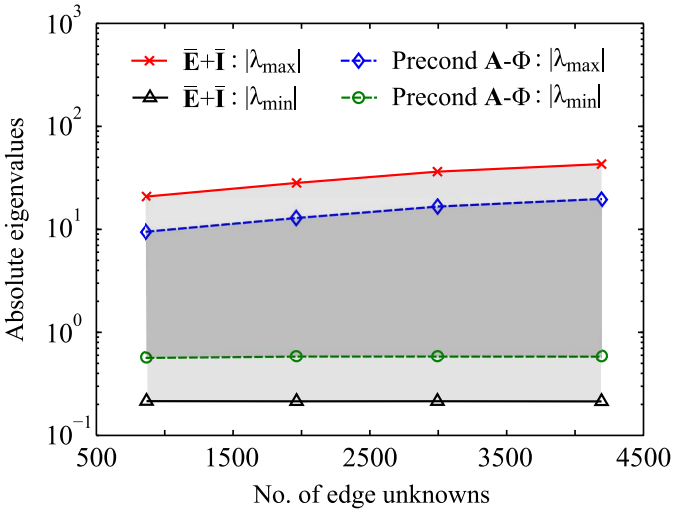

Fig. 4. Absolute eigenvalues of the A-Φ system and the matrix system $\overline{\mathbf{E}}+\overline{\mathbf{I}}$ for different mesh densities. Frequency: 300 kHz.

Clearly, the nonzero eigenvalues are approximately bounded by the spectrum of the matrix $\overline{\mathbf{E}}$ at low frequencies. Thus, the conditioning of the preconditioned A-Φ system is approximately bounded by the conditioning of $\overline{\mathbf{E}}+\overline{\mathbf{I}}$. In fact, from numerical observations of (31), at middle frequencies, the term $\tilde{\mathbf{u}}^*\overline{\mathbf{B}}^T\mathbf{v}$ is still far smaller than 1. Thus, the above conclusion can be valid even at middle frequencies.

Now, let h be the average discretization diameter. Under a certain discretization h, the zeroth order RWG basis function satisfies

$$\mathbf{f}_m = \frac{\pm l_m(\mathbf{r}_0-\mathbf{r})}{2A_m^{\pm}} = O(1) \tag{34}$$

where l_m is the RWG edge length, $\mathbf{r}_0$ and A_m are the vertex and area of the triangle, and $\mathbf{r}$ is the field point. Thus, the h-dependence of the interactions between different elements in $\overline{\mathbf{\Gamma}}_{11}$ is $O(h^4)$. This is obtained by using (34) and the double surface integral over the triangle in the matrix element evaluation in (21). Then, we have the h dependence for $\overline{\mathbf{G}}^{-1}$ as $O(h^{-4})$. Therefore

$$\overline{\mathbf{E}}+\overline{\mathbf{I}} = \overline{\mathbf{G}}^{-\frac{1}{2}}\overline{\mathbf{\Gamma}}_{11}\overline{\mathbf{G}}^{-\frac{1}{2}} = O(1) \tag{35}$$

which verifies that the elements in $\overline{\mathbf{E}}+\overline{\mathbf{I}}$ are bounded when the mesh discretization becomes denser. Actually, the spectrum of $\overline{\mathbf{G}}^{-(1/2)}\overline{\mathbf{\Gamma}}_{11}\overline{\mathbf{G}}^{-(1/2)}$ resembles that of $\overline{\mathbf{G}}^{-1}\overline{\mathbf{\Gamma}}_{11}$. The multiplication of $\overline{\mathbf{G}}^{-1}$ is a normalization procedure of the matrix elements in $\overline{\mathbf{\Gamma}}_{11}$ with respect to the mesh density.

As claimed before, the matrix $\overline{\mathbf{G}}$ is an approximation of $\overline{\mathbf{\Gamma}}_{11}$. The spectrum of $\overline{\mathbf{G}}^{-1}\overline{\mathbf{\Gamma}}_{11}$ is a continuous function between two cases. For the best case, it clusters at 1 when $\overline{\mathbf{G}} = \overline{\mathbf{\Gamma}}_{11}$. And for the simplest case when $\overline{\mathbf{G}} = \mathrm{diag}(\overline{\mathbf{\Gamma}}_{11})$, $\overline{\mathbf{G}}^{-1}$ acts as the diagonal preconditioner. Also, note that the only integral kernel in $\overline{\mathbf{\Gamma}}_{11}$ is Green's function, which is a smooth term and has substantial contribution from the self-interactions. Thus, $\overline{\mathbf{\Gamma}}_{11}$ is diagonal significant. In this way, even with $\overline{\mathbf{G}}$ being a diagonal matrix, the spectrum of the preconditioned compact operator becomes much better. As presented in Fig. 4, the spectra of the preconditioned A-Φ system are bounded by those of the matrix system $\overline{\mathbf{E}}+\overline{\mathbf{I}}$ within a finite range that is away from zero. And the A-Φ system spectrum is shown to be more compact comparing with that of $\overline{\mathbf{E}}+\overline{\mathbf{I}}$.

A similar conclusion can be drawn from the analysis using Gershgorin's disk theorem, whose applications in time domain integral equation systems can be found in [40]. Gershgorin's disk theorem [41] says that, for a complex matrix $\overline{\mathbf{V}} \in \mathbb{C}^{N\times N}$ with elements v_{ij}, the eigenvalues of $\overline{\mathbf{V}}$ locate in the disks union defined as

$$\begin{cases} \text{centers:} & v_{ii}, i = 1,\ldots,N \\ \text{radii:} & \displaystyle\sum_{j\in N\setminus i} |\, v_{ij}\,|, i = 1,\ldots,N. \end{cases} \tag{36}$$

By using (27), the preconditioned A-Φ system actually can be written into the form

$$\begin{aligned} \overline{\mathbf{V}} &= \begin{bmatrix} \overline{\mathbf{V}}_{11} & \overline{\mathbf{V}}_{12} \\ \overline{\mathbf{V}}_{21} & \overline{\mathbf{V}}_{22} \end{bmatrix} = \overline{\mathcal{P}}_c^{-1}\cdot\overline{\mathbf{\Gamma}} \\ &= \begin{bmatrix} \overline{\mathbf{G}}^{-1}\left[\overline{\mathbf{\Gamma}}_{11}-\overline{\mathbf{\Gamma}}_{21}^T\overline{\mathbf{S}}^{-1}\overline{\mathbf{\Gamma}}_{21}(\overline{\mathbf{I}}-\overline{\mathbf{G}}^{-1}\overline{\mathbf{\Gamma}}_{11})\right] & 0 \\ \overline{\mathbf{S}}^{-1}\overline{\mathbf{\Gamma}}_{21}(\overline{\mathbf{I}}-\overline{\mathbf{G}}^{-1}\overline{\mathbf{\Gamma}}_{11}) & \overline{\mathbf{I}}. \end{bmatrix}. \end{aligned} \tag{37}$$

Now, the final system matrix is in the form of a lower triangular matrix and the bottom-right block matrix is an identity matrix.

Thus, according to Gershgorin's disk theorem, the eigenvalues of the matrix $\overline{\mathbf{V}}$ can be categorized into two groups. One group belongs to the disk union made up of the first N_e rows of $\overline{\mathbf{V}}$, where N_e denotes the number of edges. Since the top-right block matrix $\overline{\mathbf{V}}_{12} = 0$, the eigenvalues in this group are actually determined by the eigenvalues of $\overline{\mathbf{V}}_{11}$. Since $\overline{\mathbf{G}}$ is the approximation of $\overline{\mathbf{\Gamma}}_{11}$, then the spectrum of $\overline{\mathbf{V}}_{11}$ resembles that of $\overline{\mathbf{G}}^{-1}\overline{\mathbf{\Gamma}}_{11}$. The other group of eigenvalues locates in the disk union associated with the remaining N_p rows of $\overline{\mathbf{V}}$, where N_p denotes the number of triangular patches. Since $\overline{\mathbf{V}}_{22} = \overline{\mathbf{I}}$, the associated disks center at 1 and the radii are determined by $\overline{\mathbf{V}}_{21}$, which vanishes as $\overline{\mathbf{G}}$ approaching $\overline{\mathbf{\Gamma}}_{11}$. This agrees with the former analysis with the generalized eigenvalue problem.

It can be concluded thereafter that the preconditioned A-Φ system has an asymptotically bounded spectrum, which indicates that the conditioning with the dense mesh discretization has been much improved after the constraint preconditioning.

E. Charge Neutrality Issue

It is demonstrated in this section that an additional benefit of the proposed constraint preconditioned A-Φ system is its immunity to the charge neutrality issue, as illustrated in [19]. In the A-EFIE, the electric current and the charge are regarded as separated unknowns, while the current continuity condition

$$\nabla\cdot\mathbf{J} = i\omega\sigma \tag{38}$$

is confined for the second equation. Typically, the charge neutrality condition is automatically satisfied due to (38) and the zero divergence of the total current by invoking Gauss' integral theorem. But at very low frequencies, it can be violated, since $\omega \approx 0$. Although we use (10) in the A-Φ

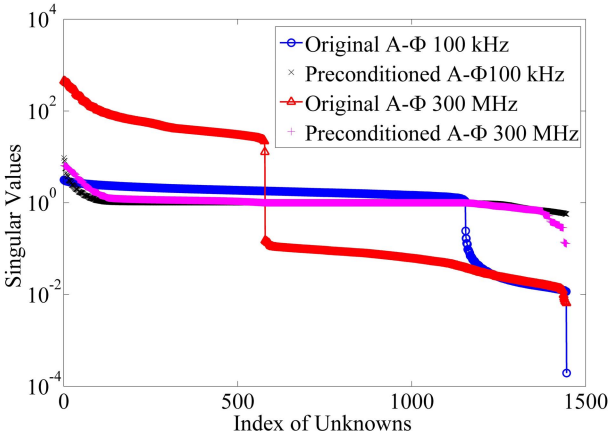

Fig. 5. Singular value distributions for **A**-Φ formulation and A-EFIE at the frequencies of 300 MHz and 100 kHz.

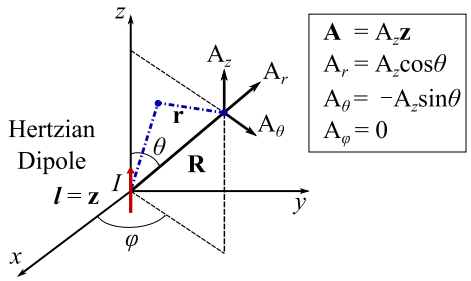

Fig. 6. Hertzian dipole with current I oriented along the z-axis.

formulation, our system matrix resembles that of the A-EFIE and still has such an electrostatic nullspace.

Here, an example is used to present the singular value distribution of the **A**-Φ system with and without left constraint preconditioner. We use the same PEC sphere example as that in IV-C. The singular value spectra are plotted at the frequency of 300 MHz and 100 kHz, as shown in Fig. 5. For middle frequency such as 300 MHz, no extremely small singular values are found. When the frequency lowers, there exists one very small singular value compared with others. It is observed that after preconditioning, not only the spectrum is smoothed but also the smallest singular value corresponding to the nullspace disappears.

V. Incident Potentials

A. Hertzian Dipole and Plane-Wave Incident

For near-field excitation, as shown in Fig. 6, a Hertzian dipole with current $\mathbf{J}(\mathbf{r}) = Il\hat{\ell}\delta(\mathbf{r})$ is oriented along the z-axis and placed as a point source near an object with coordinate $(r, \theta, \boldsymbol{\phi})$. Then, the incident vector potential is

$$\mathbf{A}_{\text{inc}} = \mu Il\hat{\ell}\frac{e^{\text{ikr}}}{4\pi r}. \tag{39}$$

The incident scalar potential can be obtained from the Lorenz gauge

$$\begin{aligned} i\omega\epsilon\Phi_{\text{inc}} &= \nabla\cdot\mathbf{A}_{\text{inc}}/\mu \\ &= Il\frac{(-e^{\text{ikr}} + ikre^{\text{ikr}})\cos\theta}{4\pi r^2}. \end{aligned} \tag{40}$$

Thus, the vector potential is only related to the distance from the source, while the scalar potential is dependent on the location with both r and θ. And the second term in (40) can be omitted as r becomes small in the near field.

An incident plane wave can be defined from the spherical wave of the Hertzian dipole radiating from the far field. The incident vector potential can be approximated as

$$\mathbf{A}_{\text{inc}} = \mu Il\hat{\ell}\frac{e^{ik|\mathbf{R}+\mathbf{r}|}}{4\pi\,|\,\mathbf{R}+\mathbf{r}\,|} \approx \mu Il\hat{\ell}\frac{e^{\text{ikr}}}{4\pi r}e^{i\mathbf{k}_i\cdot\mathbf{r}}, \quad |\,\mathbf{R}\,| \gg |\,\mathbf{r}\,|\,. \tag{41}$$

Subsequently, it can be written in terms of two components with $\mathbf{a}_\perp$ perpendicular to the wave propagation direction and $\mathbf{a}_\parallel$ the longitudinal component, namely

$$\mathbf{A}_{\text{inc}} = (\mathbf{a}_\perp + \mathbf{a}_\parallel)e^{i\mathbf{k}_i\cdot\mathbf{r}} \tag{42}$$

where $\mathbf{k}_i$ is along the $\mathbf{r}$ direction. The two components indicate the incident angle of the vector potential. The scalar potentials can be derived accordingly as follows:

$$i\omega\epsilon\Phi_{\text{inc}} = \nabla\cdot\mathbf{A}_{\text{inc}}/\mu = \frac{i}{\mu}\mathbf{k}_i\cdot\mathbf{a}_\parallel e^{i\mathbf{k}_i\cdot\mathbf{r}}. \tag{43}$$

The longitudinal component vanishes in the incident scalar potential. Under the perpendicular incidence of the vector potential, $\mathbf{a}_\parallel = 0$. The incident scalar potential equals to zero, which could happen in the broadside direction of a dipole. This is also known as the $\Phi = 0$ gauge or radiation gauge. These incident potentials defined by the Hertzian dipole can be proved to reveal the incident electric field of plane wave as

$$\begin{aligned} \mathbf{E}_{\text{inc}} &= i\omega\mathbf{A}_{\text{inc}} - \nabla\Phi_{\text{inc}} = i\omega\mathbf{A}_{\text{inc}} - \frac{\nabla\nabla\cdot\mathbf{A}_{\text{inc}}}{i\omega\mu\epsilon} \\ &= -\frac{i\mathbf{k}_i\times(i\mathbf{k}_i\times\mathbf{A}_{\text{inc}})}{i\omega\mu\epsilon} = i\omega\mathbf{a}_\perp e^{i\mathbf{k}_i\cdot\mathbf{r}}, \end{aligned} \tag{44}$$

and the magnetic field

$$\mathbf{B}_{\text{inc}} = \nabla\times\mathbf{A}_{\text{inc}} = i\mathbf{k}_i\times\mathbf{a}_\perp e^{i\mathbf{k}_i\cdot\mathbf{r}}. \tag{45}$$

The existence of the longitudinal component in $\mathbf{A}_{\text{inc}}$ indicates that the potential still exists even if both $\mathbf{E}_{\text{inc}}$ and $\mathbf{H}_{\text{inc}}$ are zero.

B. Local Source Excitation

For circuit problems, a local excitation with delta-gap source is desired. It is an approximation of an impressed uniform electric field between the thin gaps. However, it is difficult to directly compute the potentials from the impressed electric field due to the discontinuity of the field. Actually, the circuit can be excited by an arbitrary impressed field at the port area and then gradually becomes stable. The electric field $\mathbf{E}_{\text{inc}} = i\omega\mathbf{A}_{\text{inc}} - \nabla\Phi_{\text{inc}}$, where $\mathbf{A}_{\text{inc}}$ denotes the contribution from the current, while Φ_{inc} denotes the contribution from the charge. A scalar potential-based excitation can be found in [43].

The physical meaning here for the delta-gap source is different from that in [43]. As illustrated in Fig. 7, a toroidal solenoid with slow-varying current provides a quasi-magnetostatic field, which is trapped inside the solenoid.

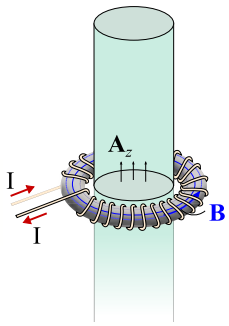

Fig. 7. Vector potential-based local excitation at the port area.

Outside the solenoid, $\mathbf{B} = 0$, and however, the potential $\mathbf{A}$ still exists. The magnetic dipole works as the primary winding in a transformer. Due to the existence of the vector potential, the electrical dipole gets excited as a secondary winding. Similar to the definition of voltage delta-gap source [44], in order to simplify the computation cost, a potential-based delta-gap source approximation is defined here with

$$\boldsymbol{\alpha}_{\text{inc}}(\mathbf{r}) = \begin{cases} \boldsymbol{\alpha}_0, & \mathbf{r} \text{ in the port area} \\ 0, & \text{otherwise} \end{cases} \tag{46}$$

where one can attach each port to a given potential $\boldsymbol{\alpha}_{\text{inc}} = \boldsymbol{\alpha}_0$, while the potentials for the rest of the edges are set to be 0. If multiple ports are defined for a problem at different locations, one can even attach a constant potential to a given port and grounding the others. By this way, the port information, such as input impedance, can be easily obtained for each port, respectively. The source does not have a Φ_{inc} contribution, since there is no charge accumulation.

Assuming the gap width of the delta-gap model to be Δ_z, the port voltage V then can be computed from the electric field

$$V = \mathbf{E}_{\text{inc}} \cdot \Delta_z \hat{\mathbf{z}} = i\omega \mathbf{A}_{\text{inc}} \cdot \Delta_z \hat{\mathbf{z}}. \tag{47}$$

Since the vector potential is originally generated by a current in the toroidal solenoid, the source defined by $\mathbf{A}$ can be understood as the voltage source generated by the currents. The input impedance can be obtained accordingly after solving the integral equation.

VI. Large-Scale Computations

It is to be noted that the only integral kernel in the $\mathbf{A}$-Φ formulation is the scalar Green's function, which enables the easy integration of existing FMAs. Then, it is possible for us to use the $\mathbf{A}$-Φ formulation to solve real-world large-scale problems efficiently. In this paper, we incorporate the mixed-form FMA that expands the field with mutipoles at low frequencies and with plane waves at middle frequencies [45].

On the other hand, the fast computation with respect to the preconditioner is another important issue. As indicated in (27), the computation cost for the preconditioner is determined by the computation of $\overline{\mathbf{S}}^{-1}$. The Schur complement $\overline{\mathbf{S}}$ is originally a dense matrix. There are mature mathematical techniques to quickly obtain an inverse of a sparse matrix. Due to the scalar Green's function, the self-interactions are significant in all the block matrices $\overline{\mathbf{\Gamma}}_{ij}, (i, j = 1, 2)$. Then, the fast approximate inverse of $\overline{\mathbf{S}}$ can be achieved by taking the sparse matrix as

$$\overline{\mathbf{S}}' = k_0^2 \text{diag}(\overline{\mathbf{\Gamma}}_{22}) - \text{diag}(\overline{\mathbf{\Gamma}}_{21}) \cdot \overline{\mathbf{G}}^{-1} \cdot \text{diag}(\overline{\mathbf{\Gamma}}_{21}^T) \tag{48}$$

where the notation "diag" denotes taking the diagonal elements. Here, $\overline{\mathbf{\Gamma}}_{21}$ is not a square matrix, so the elements in $\text{diag}(\overline{\mathbf{\Gamma}}_{21})$ and $\text{diag}(\overline{\mathbf{\Gamma}}_{21}^T)$ denote the self-interaction terms between the patches and their edges. Here, we use the multi-frontal method as a fast direct solver to obtain the approximate inverse of the Schur complement. The diagonal scheme can also be applied on the matrix $\overline{\mathbf{\Gamma}}_{21}$ in (27).

Typically, the computational complexity of the $\mathbf{A}$-Φ formulation solver, including the preconditioner part, can be achieved as proportional to $N \log N$, where N is the number of unknowns ($N = N_{\text{edges}} + N_{\text{patches}}$).

Some tradeoffs on the convergence are expected when the sparse scheme is applied on the preconditioner. Here, we apply the lease cost way to build the constraint preconditioner by taking the diagonals only to observe its performance limit. For better clarification, we denote the system with preconditioner (27) as "preconditioned $\mathbf{A}$-Φ" and the system with sparse approximation in the preconditioner as "sparse preconditioned $\mathbf{A}$-Φ." The comparison between these two preconditioning strategies will be given in the numerical results.

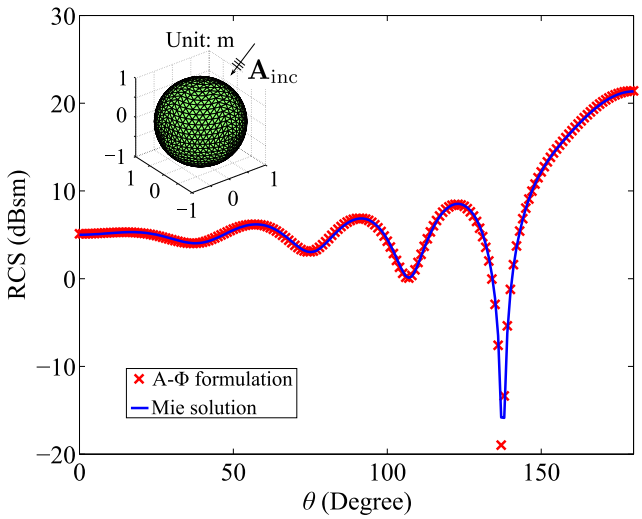

Fig. 8. Far-field RCS result for a unit PEC sphere at 300 MHz.

VII. Numerical Results

A. Plane-Wave Scattering

1) PEC Sphere: The scattering of a unit PEC sphere is shown here. When the unknown number is not large, the $\mathbf{A}$-Φ formulation can be solved using a direct method without a preconditioner. The system can achieve good accuracy until very low frequencies. Figs. 8 and 9 plot the scattering cross section results for the PEC sphere at 300 MHz and 50 Hz, respectively ($\Phi_{\text{inc}} \neq 0$). The results solved by the $\mathbf{A}$-Φ formulation match well with the analytical solutions.

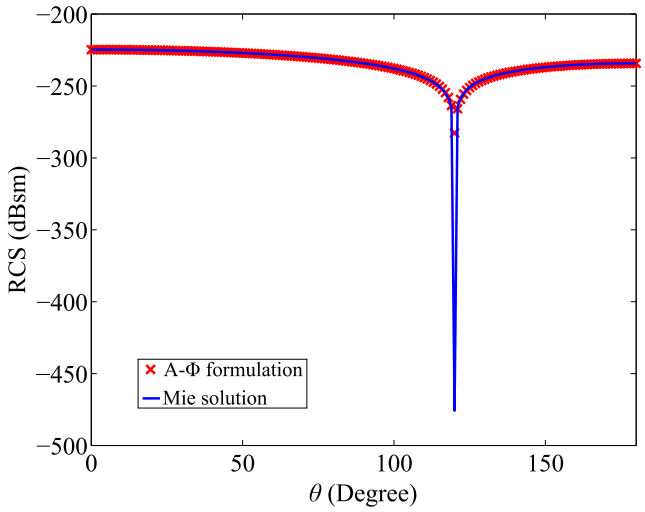

Fig. 9. Far-field RCS result for a unit PEC sphere at 50 Hz.

TABLE I

NUMBER OF ITERATIONS FOR A-EFIE AND **A**-Φ SYSTEMS FOR A SPHERE MODEL WITH 867 UNKNOWNS. TOL = 10^{-7}

Freq (MHz)	A-EFIE	$\overline{\mathbf{M}}^{-1}$·A-EFIE	**A**-Φ	$\overline{\mathcal{P}}_c^{-1}\cdot$ (**A**-Φ)
100	266	40	463	34
10	186	29	179	20
1	168	28	164	16
0.1	160	28	211	9

TABLE II

NUMBER OF ITERATIONS FOR DIFFERENT METHODS FOR A SPHERE MODEL WITH 2352 UNKNOWNS. TOL = 10^{-7}

Freq (MHz)	A-EFIE	$\overline{\mathbf{M}}^{-1}$·A-EFIE	**A**-Φ	$\overline{\mathcal{P}}_c^{-1}\cdot$ (**A**-Φ)
100	330	46	645	32
10	238	35	196	22
1	206	34	170	17
0.1	195	34	212	10

While the iterative solver is employed, Tables I and II present the iteration numbers for different methods at different frequencies. Here, the restarted GMRES method with a restart number of 50 (denoted as GMRES-50) is incorporated. The error tolerance for the iterative solver is 10^{-7}. In Table I, the sphere is discretized with 578 triangle patches and 867 edges. It is shown that, without preconditioners, the convergence of the **A**-Φ formulation is better than the A-EFIE; however, it is unstable at higher or lower frequencies. The system can be efficiently stabilized by the $\mathcal{P}_c^{-1}$ preconditioner, which is especially effective and converges much faster than the A-EFIE at low frequencies. Here, the inverse of the Schur complement is obtained by using the direct solver. Table II describes the iteration information of the scattering for a PEC sphere, which is discretized into 1568 triangle patches and 2352 edges. From the results, it can be concluded that the **A**-Φ formulation after preconditioning shows a better performance over the original A-EFIE for denser meshes. Although the system is not free from interior resonance problem at high frequencies, it presents a fast and stable convergence regardless of the increase of the unknown number at low frequencies.

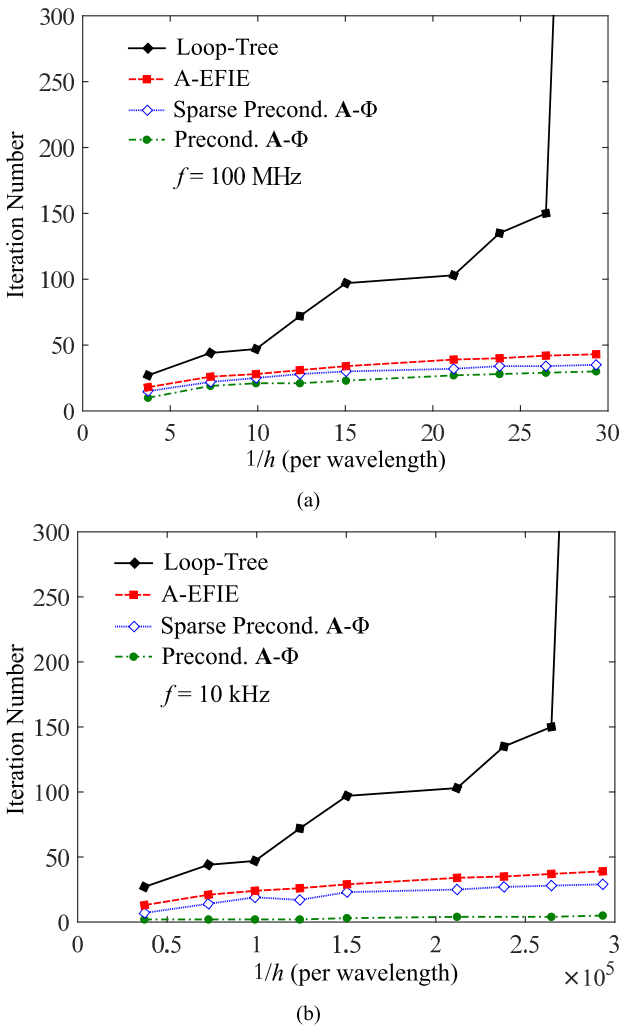

Fig. 10. Number of iterations for different solvers with mesh densities at different frequencies. (a) $f = 100$ MHz. (b) $f = 10$ kHz (a unit PEC cube).

2) PEC Cube: Further results with various mesh densities are computed with a PEC cube whose shape does not change with different discretizations. The cube has a side length of 1 m. Also, the comparison between the **A**-Φ formulation with and without sparse preconditioning approximation is given. Fig. 10(a) shows the iteration number of different solvers with mesh densities at 100 MHz (with the total electrical size of 0.33λ). Here, an iterative solver with GMRES-50 is used, and h denotes the average discretized triangle edge length. A standard loop-tree decomposition method (with frequency normalization) is shown here for comparison, and it fails to converge when the discretization becomes denser, while the systems with A-EFIE and **A**-Φ formulation (both with constraint preconditioner) achieve stable convergence.

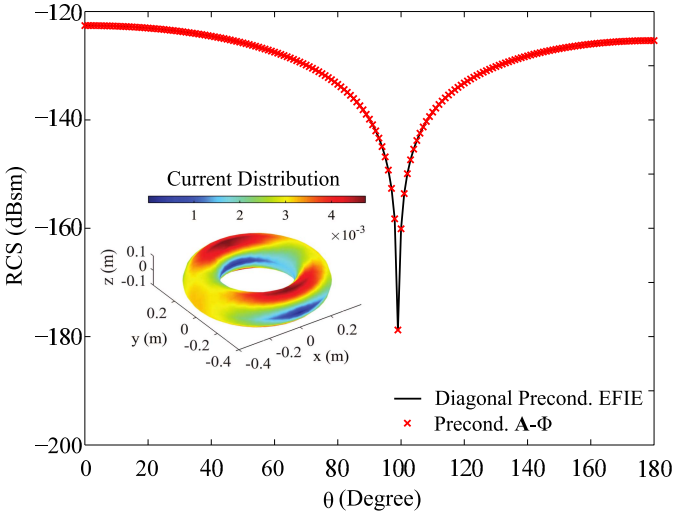

Fig. 11. Far-field results of a PEC torus computed from EFIE and **A**-Φ formulation and the current distribution solved with the **A**-Φ formulation. Frequency: 100 kHz.

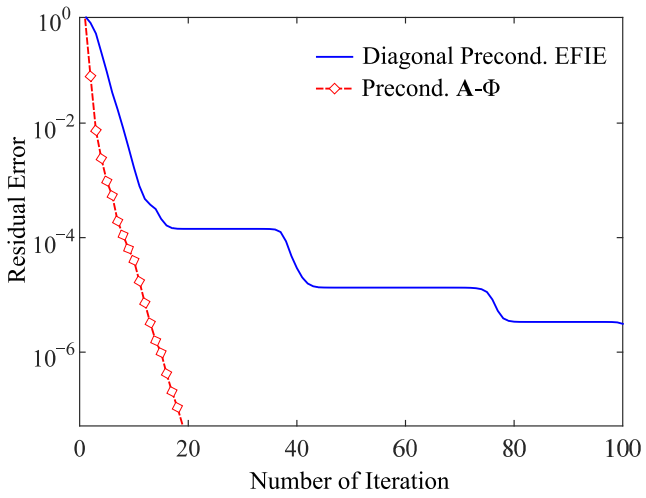

Fig. 12. Convergence results of a PEC torus computed from the EFIE and **A**-Φ formulation. Frequency: 100 kHz.

The sparse preconditioned **A**-Φ formulation shows quite a slower convergence compared with the original precondtioned one. Also, it is noted that both of them show a better performance over the A-EFIE on the convergence rate. The advantage becomes more significant when the frequency is lower, especially for the original precodntioned **A**-Φ formulation, as shown in Fig. 10(b) with the frequency of 10 kHz (with the total electrical size of $0.33 \times 10^{-4}\lambda$).

3) Multiply-Connected Structure: The computation of multiply-connected structures recently gains much attention for the existence of magnetostatic nullspaces at the static limit. EFIEs do not suffer from this problem. Physically, the potential-based integral equation is also immune from this nullspace problem, because, as in the cases of Aharonov–Bohm effect, the potentials still exist and describe the physics even with a null magnetic field.

Here, a one-genus toroidal structure is presented to validate the accuracy of **A**-Φ formulation in solving multiply-connected problems. The total dimension of the object is 0.8 m × 0.8 m × 0.2 m, and the radius of the torus tube is 0.1 m. The model is discretized into 1076 triangle patches with 1614 edges. The working frequency is chosen to be a low frequency at 100 kHz. Under a plane-wave excitation, as shown in Fig. 11, the far-field scattering results of **A**-Φ formulation agrees well with that computed with the EFIE. The subfigure in Fig. 11 plots the current distribution on the torus surface, which also matches well with that solved from EFIE. With the constraint preconditioner, the **A**-Φ formulation achieves a much better convergence (GMRES-50), as shown in Fig. 12.

4) NASA Almond: We then consider a NASA almond with the dimension of $3.37\lambda \times 1.30\lambda \times 0.43\lambda$ at 4 GHz. The structure contains sharp edges and a pointed corner. It is discretized into 2907 edges and 1938 triangle patches, as shown in Fig. 13(a). The simple EFIE is capable of handling the accuracy for computing such a problem. Fig. 13(b) plots the far-field

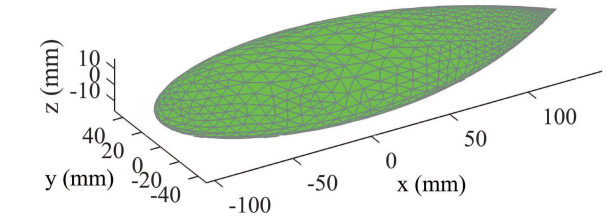

(a)

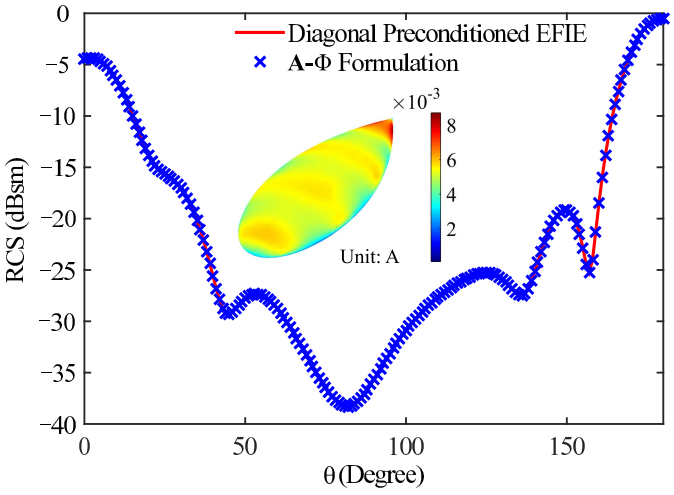

(b)

Fig. 13. (a) Geometry and discretization of the NASA almond model. (b) Far-field result and the current distribution of the almond at 4 GHz.

scattering results for the **A**-Φ formulation and the diagonal preconditioned EFIE, which match well with each other. The image in the center of Fig. 13(b) shows the current distribution on the almond surface. With the constraint preconditioner, the **A**-Φ formulation can converge in 98 iteration steps for a GMRES-100 iterative solver with an error tolerance of 10^{-7}, while the EFIE converges to the same error tolerance after 5000 iteration steps.

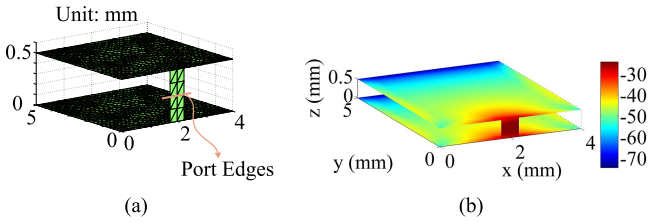

Fig. 14. (a) Geometry of the parallel-plate capacitor model. (b) Current distribution of the capacitor at 10 MHz. Unit: $20\log_{10}$(A/m).

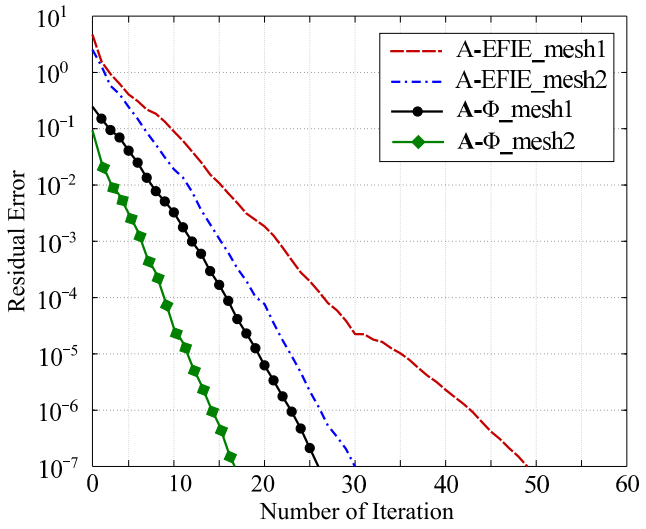

Fig. 15. Iteration information of the parallel-plate capacitor for different meshes using the A-EFIE and **A**-Φ formulation (both with constraint preconditioners).

B. Electrostatic Problem

For the electrostatic problem, an example of a 5 mm × 4 mm × 0.5 mm parallel-plate capacitor is considered. As presented in Fig. 14(a), the capacitor is discretized into 2288 edges and 1576 triangle patches. A potential-based delta-gap source is applied in the central edges of the connected bridge between the two plates. Fig. 14(b) shows the current distribution of the capacitor solved using the **A**-Φ formulation. The current is largest at the port area and then gradually vanishes to the open end. Using the input impedance at port edges, the capacitance is calculated to be 0.47 pF, which is the same as the A-EFIE result. The convergence information of two different mesh densities is compared in Fig. 15 for the A-EFIE and **A**-Φ formulation at 10 MHz. Mesh 1 is denser with 2288 edges, while mesh 2 has for 553 edges. The **A**-Φ method converges much faster than the A-EFIE method regardless of the mesh densities.

C. Magnetostatic Problem

The magnetostatic problem is discussed here with a strip loop inductor, as shown in Fig. 16. This is also a multiply-connected structure. Generally, the magnetostatic nullspace problems should be considered more carefully in the local-excited multiply-connected structures than in the scattering problems, since lumped elements usually work at low

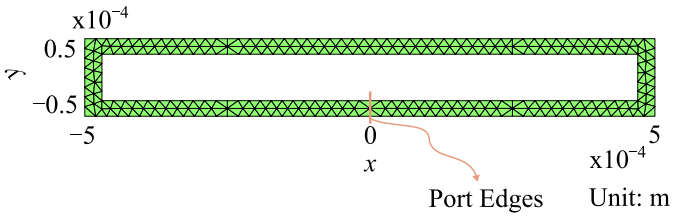

Fig. 16. Model of a rectangular loop structure.

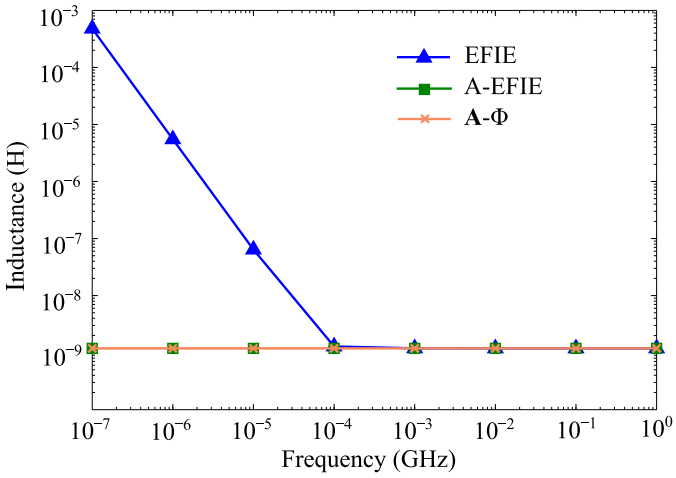

Fig. 17. Comparison of computed inductance for the EFIE, A-EFIE, and **A**-Φ formulation.

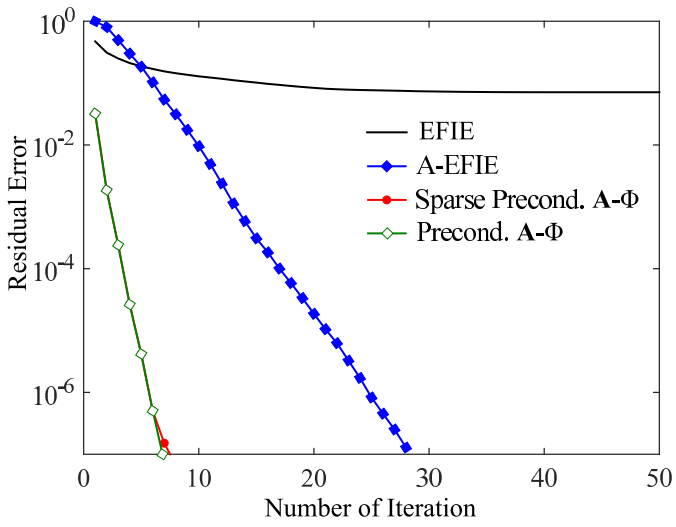

Fig. 18. Convergence results for the strip loop using the EFIE, A-EFIE, and **A**-Φ formulation.

frequencies and the global-loop currents are very important modal counterparts in local-excited problem solutions. Here, the loop inductor is discretized into 1017 edges and 678 triangle patches. Similar to the case of the capacitor, a potential-based delta-gap source is assigned in the middle of the bottom side. In Fig. 17, the inductance is calculated according to input impedance for the EFIE, A-EFIE, and **A**-Φ formulation, respectively. The computed inductance using the three methods matches well with each other at higher

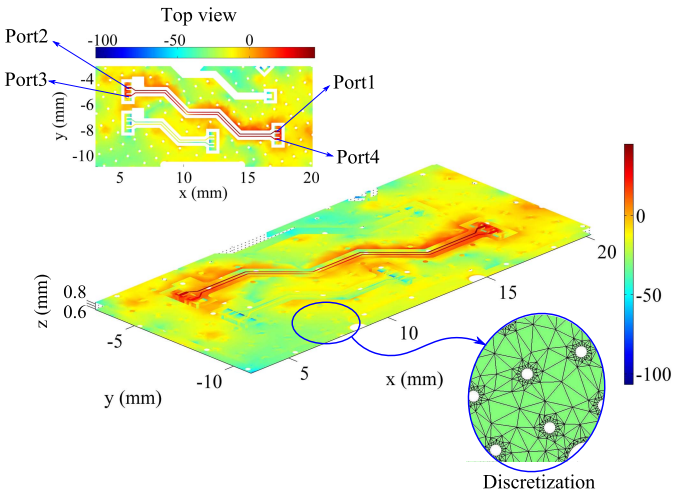

Fig. 19. Current distribution of the four-port interconnects under the delta-gap excitation at port 1. Frequency: 20 GHz. Unit: $20\log_{10}$(A/m). The top view of the current distribution and the discretization are shown in subfigures.

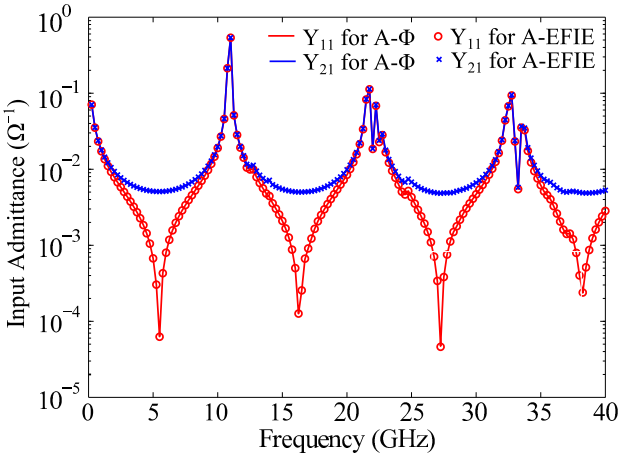

Fig. 20. Magnitude of the input impedances Y_{11} and Y_{21} solved with the A-EFIE and **A**-Φ formulation.

frequencies until several hundreds of kilohertz. As frequencies continually lower, a low-frequency breakdown problem starts to emerge in the EFIE, and the computed inductance begins to diverge. The result from the **A**-Φ formulation still remains stable until very low frequencies and shows good agreement with that of the A-EFIE. At the frequency of 10^{-5} GHz, when the EFIE does not converge due to low-frequency breakdown, our proposed method still converges well and better than the A-EFIE, as shown in Fig. 18.

D. Four-Port Interconnects System

A four-port board plate structure with two pairs of interconnects is presented here. The structure is a part cut from a realistic package board, which is discretized into 27 315 inner edges and 19 870 triangle patches. Fig. 19 shows the current distribution on the metallic board at 20 GHz with the delta-gap excitation at port 1. The image presented in the blue ellipse on the bottom-right of Fig. 19 describes the multiscale discretization with the mesh elements of maximum edge length $\lambda/10$ and minimum edge length $\lambda/3000$.

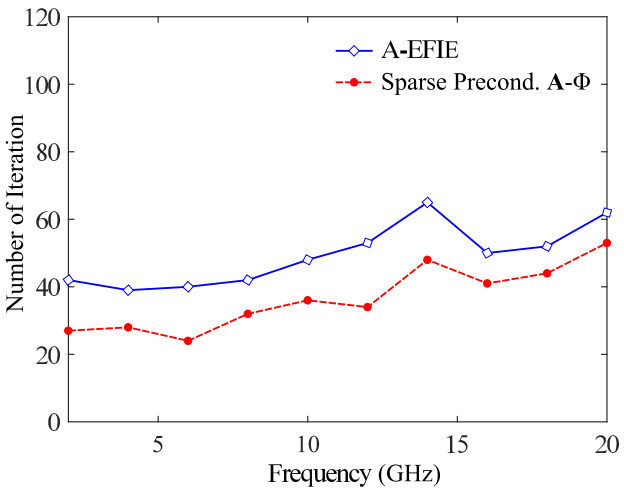

Fig. 21. Convergence information for the four-port interconnects problem solved with the A-EFIE and **A**-Φ formulation.

Fig. 20 plots the magnitude of the input impedances Y_{11} and Y_{21} from 0.25 to 40 GHz with 160 frequency points. The results agree well with those calculated with the A-EFIE method. Here, a mixed-form multilayer FMA with five layers is incorporated in the solver, and the average iteration step is approximately to be 40 for each frequency point (GMRES-100, error tolerance: 10^{-3}).

Also, the convergence information is plotted here by sweeping the frequency from 2 to 20 GHz. As shown in Fig. 21, the sparse preconditioned **A**-Φ formulation shows an advantage over the A-EFIE (with constraint preconditioner) on the convergence over a wide range of frequencies.

VIII. Conclusion

In this paper, an integral form of the potential-based formulation has been proposed and implemented to solve EM problems over a wideband frequency range. The system, which is applicable to both scattering and circuit problems, has been validated as immune to the low-frequency catastrophe, the ill-conditioning with dense mesh, and the magnetostatic nullspace problem. The integral kernel of the formulation is just Green's function; thus, it is convenient to incorporate existing fast solvers to solve real-world problems with a large number of unknowns. Since the equation is formulated with potentials instead of fields, and works well for long-wavelength situations, it is possible to couple with the quantum theory to solve quantum effects problems where the problem sizes are usually much smaller compared with the wavelength.

References

[1] W. Chew, M.-S. Tong, and B. Hu, *Integral Equation Methods for Electromagnetic and Elastic Waves*. San Rafael, CA, USA: Morgan & Claypool, 2008.

[2] F. P. Andriulli, A. Tabacco, and G. Vecchi, "Solving the EFIE at low frequencies with a conditioning that grows only logarithmically with the number of unknowns," *IEEE Trans. Antennas Propag.*, vol. 58, no. 5, pp. 1614–1624, May 2010.

[3] J.-S. Zhao and W. C. Chew, "Integral equation solution of Maxwell's equations from zero frequency to microwave frequencies," *IEEE Trans. Antennas Propag.*, vol. 48, no. 10, pp. 1635–1645, Oct. 2000.

[4] D. R. Wilton and A. W. Glisson, "On improving the stability of the electric field integral equation at low frequencies," in *Proc. URSI Radio Sci. Meeting*, Los Angeles, CA, USA, Jun. 1981, p. 24.

[5] J. R. Mautz and R. Harrington, "An E-field solution for a conducting surface small or comparable to the wavelength," *IEEE Trans. Antennas Propag.*, vol. AP-32, no. 4, pp. 330–339, Apr. 1984.

[6] G. C. Hsiao and R. E. Kleinman, "Mathematical foundations for error estimation in numerical solutions of integral equations in electromagnetics," *IEEE Trans. Antennas Propag.*, vol. 45, no. 3, pp. 316–328, Mar. 1997.

[7] H. Contopanagos *et al.*, "Well-conditioned boundary integral equations for three-dimensional electromagnetic scattering," *IEEE Trans. Antennas Propag.*, vol. 50, no. 12, pp. 1824–1830, Dec. 2002.

[8] R. J. Adams, "Physical and analytical properties of a stabilized electric field integral equation," *IEEE Trans. Antennas Propag.*, vol. 52, no. 2, pp. 362–372, Feb. 2004.

[9] A. Buffa and S. Christiansen, "A dual finite element complex on the barycentric refinement," *Math. Comput.*, vol. 76, pp. 1743–1769, May 2007.

[10] F. P. Andriulli *et al.*, "A multiplicative Calderón preconditioner for the electric field integral equation," *IEEE Trans. Antennas Propag.*, vol. 56, no. 8, pp. 2398–2412, Aug. 2008.

[11] M. B. Stephanson and J.-F. Lee, "Preconditioned electric field integral equation using Calderón identities and dual loop/star basis functions," *IEEE Trans. Antennas Propag.*, vol. 57, no. 4, pp. 1274–1279, Apr. 2009.

[12] S. Yan, J.-M. Jin, and Z. Nie, "EFIE analysis of low-frequency problems with loop-star decomposition and Calderón multiplicative preconditioner," *IEEE Trans. Antennas Propag.*, vol. 58, no. 3, pp. 857–867, Mar. 2010.

[13] F. P. Andriulli, "Loop-star and loop-tree decompositions: Analysis and efficient algorithms," *IEEE Trans. Antennas Propag.*, vol. 60, no. 5, pp. 2347–2356, May 2012.

[14] K. Cools, F. P. Andriulli, F. Olyslager, and E. Michielssen, "Nullspaces of MFIE and Calderón preconditioned EFIE operators applied to toroidal surfaces," *IEEE Trans. Antennas Propag.*, vol. 57, no. 10, pp. 3205–3215, Oct. 2009.

[15] F. P. Andriulli, K. Cools, I. Bogaert, and E. Michielssen, "On a well-conditioned electric field integral operator for multiply connected geometries," *IEEE Trans. Antennas Propag.*, vol. 61, no. 4, pp. 2077–2087, Apr. 2013.

[16] J. Zhu, S. Omar, and D. Jiao, "Solution of the electric field integral equation when it breaks down," *IEEE Trans. Antennas Propag.*, vol. 62, no. 8, pp. 4122–4134, Aug. 2014.

[17] M. Taskinen and P. Ylä-Oijala, "Current and charge integral equation formulation," *IEEE Trans. Antennas Propag.*, vol. 54, no. 1, pp. 58–67, Jan. 2006.

[18] D. Gope, A. Ruehli, and V. Jandhyala, "Solving low-frequency EM-CKT problems using the PEEC method," *IEEE Trans. Adv. Packag.*, vol. 30, no. 2, pp. 313–320, May 2007.

[19] Z. G. Qian and W. C. Chew, "Fast full-wave surface integral equation solver for multiscale structure modeling," *IEEE Trans. Antennas Propag.*, vol. 57, no. 11, pp. 3594–3601, Nov. 2009.

[20] Y. Xu, R. J. Adams, and S. D. Gedney, "A Nyström implementation of an augmented electric field integral equation for low frequency electrical analysis," in *Proc. IEEE Int. Symp. Antennas Propag.*, Charleston, SC, USA, Jun. 2009, pp. 1–4.

[21] J. C. Young, Y. Xu, R. J. Adams, and S. D. Gedney, "High-order Nyström implementation of an augmented electric field integral equation," *IEEE Antennas Wireless Propag. Lett.*, vol. 11, pp. 846–849, 2012.

[22] J. Cheng and R. J. Adams, "Electric field-based surface integral constraints for Helmholtz decompositions of the current on a conductor," *IEEE Trans. Antennas Propag.*, vol. 61, no. 9, pp. 4632–4640, Sep. 2013.

[23] S. Gasiorowicz, *Quantum Physics*. New York, NY, USA: Wiley, 2007.

[24] N. A. Demerdash, F. A. Fouad, T. W. Nehl, and O. A. Mohammed, "Three dimensional finite element vector potential formulation of magnetic fields in electrical apparatus," *IEEE Trans. Power App. Syst.*, vol. PAS-100, no. 8, pp. 4104–4111, Aug. 1981.

[25] O. Biro and K. Preis, "On the use of the magnetic vector potential in the finite-element analysis of three-dimensional eddy currents," *IEEE Trans. Magn.*, vol. 25, no. 4, pp. 3145–3159, Jul. 1989.

[26] B. E. MacNeal, J. R. Brauer, and R. N. Coppolino, "A general finite element vector potential formulation of electromagnetics using a time-integrated electric scalar potential," *IEEE Trans. Magn.*, vol. 26, no. 5, pp. 1768–1770, Sep. 1990.

[27] R. Dyczij-Edlinger, G. Peng, and J.-F. Lee, "A fast vector-potential method using tangentially continuous vector finite elements," *IEEE Trans. Microw. Theory Techn.*, vol. 46, no. 6, pp. 863–868, Jun. 1998.

[28] P. Dular, J. Gyselinck, C. Geuzaine, N. Sadowski, and J. P. A. Bastos, "A 3-D magnetic vector potential formulation taking eddy currents in lamination stacks into account," *IEEE Trans. Magn.*, vol. 39, no. 3, pp. 1424–1427, May 2003.

[29] P. De Doncker, "A volume/surface potential formulation of the method of moments applied to electromagnetic scattering," *Eng. Anal. Boundary Elements*, vol. 27, no. 4, pp. 325–331, 2003.

[30] F. Vico, L. Greengard, M. Ferrando, and Z. Gimbutas, "The decoupled potential integral equation for time-harmonic electromagnetic scattering," *Commun. Pure Appl. Math.*, vol. 69, no. 4, pp. 771–812, Apr. 2016.

[31] W. C. Chew, "Vector potential electromagnetics with generalized gauge for inhomogeneous media: Formulation (invited paper)," *Prog. Electromagn. Res.*, vol. 149, pp. 69–84, 2014.

[32] Q. S. Liu, S. Sun, and W. C. Chew, "A vector potential integral equation method for electromagnetic scattering," in *Proc. Int. Rev. Prog. Appl. Comput. Electromagn. (ACES)*, Mar. 2015, pp. 1–2.

[33] Q. S. Liu, S. Sun, and W. C. Chew, "An integral equation method based on vector and scalar potential formulations," in *Proc. IEEE Int. Symp. Antennas Propag.*, Jul. 2015, pp. 744–745.

[34] J. D. Jackson, *Classical Electrodynamics*. San Rafael, CA, USA: Morgan & Claypool, 2008.

[35] W. C. Chew, *Waves and Fields in Inhomogenous Media* (First Published in 1990 by Van Nostrand Reinhold), vol. 522. New York, NY, USA: IEEE Press, 1995.

[36] O. Ergül and L. Gürel, *The Multilevel Fast Multipole Algorithm (MLFMA) for Solving Large-Scale Computational Electromagnetics Problems*. New York, NY, USA: Wiley, 2014.

[37] J. Cheng, R. J. Adams, J. C. Young, and M. A. Khayat, "Augmented EFIE with normally constrained magnetic field and static charge extraction," *IEEE Trans. Antennas Propag.*, vol. 63, no. 11, pp. 4952–4963, Nov. 2015.

[38] M. Benzi, G. H. Golub, and J. Liesen, "Numerical solution of saddle point problems," *Acta Nemurica*, vol. 14, pp. 1–137, Apr. 2005.

[39] C. Keller, N. I. M. Gould, and A. J. Wathen, "Constraint preconditioning for indefinite linear systems," *SIAM J. Matrix Anal. Appl.*, vol. 21, no. 4, pp. 1300–1317, 2000.

[40] F. P. Andriulli, H. Bagci, F. Vipiana, G. Vecchi, and E. Michielssen, "Analysis and regularization of the TD-EFIE low-frequency breakdown," *IEEE Trans. Antennas Propag.*, vol. 57, no. 7, pp. 2034–2046, Jul. 2009.

[41] R. S. Varga, *Geršgorin and His Circles*. Berlin, Germany: Springer-Verlag, 2004.

[42] O. Axelsson and M. Neytcheva, "Preconditioning methods for linear systems arising in constrained optimization problems," *Numer. Linear Algebra Appl.*, vol. 10, nos. 1–2, pp. 3–31, 2003.

[43] S. Omar and D. Jiao, "A new volume integral formulation for broadband 3-D circuit extraction in inhomogeneous materials with and without external electromagnetic fields," *IEEE Trans. Microw. Theory Techn.*, vol. 61, no. 12, pp. 4302–4312, Dec. 2013.

[44] Y. H. Lo, L. J. Jiang, and W. C. Chew, "Finite-width feed and load models," *IEEE Trans. Antennas Propag.*, vol. 61, no. 1, pp. 281–289, Jan. 2013.

[45] L. J. Jiang and W. C. Chew, "A mixed-form fast multipole algorithm," *IEEE Trans. Antennas Propag.*, vol. 53, no. 12, pp. 4145–4156, Dec. 2005.

Qin S. Liu (S'12–M'16) received the B.Eng. degree in electronic engineering from the University of Science and Technology of China, Hefei, China, in 2011, and the Ph.D. degree in electrical and electronic engineering from The University of Hong Kong, Hong Kong, in 2015.

She is currently a Post-Doctoral Fellow in electrical and electronic engineering with The University of Hong Kong. Her current research interests include numerical methods and fast algorithms in computational electromagnetics.

Sheng Sun (S'02–M'07–SM'12) received the B.Eng. degree in information engineering from Xi'an Jiaotong University, Xi'an, China, in 2001, and the Ph.D. degree in electrical and electronic engineering from Nanyang Technological University (NTU), Singapore, in 2006.

From 2005 to 2006, he was with the Institute of Microelectronics, Singapore. From 2006 to 2008, he was a Post-Doctoral Research Fellow with NTU. He was a Humboldt Research Fellow with the Institute of Microwave Techniques, University of Ulm, Ulm, Germany, from 2008 to 2010, and a Research Assistant Professor with The University of Hong Kong, Hong Kong, from 2010 to 2015. Since 2015, he has been the Young Thousand Talents Plan Professor with the University of Electronic Science and Technology of China, Chengdu, China. He has co-authored one book and two book chapters, and over 140 journal and conference publications. His current research interests include electromagnetic theory, computational mathematics, multiphysics, numerical modeling of planar circuits and antennas, microwave passive and active devices, and the microwave- and millimeter-wave communication systems.

Dr. Sun is currently a member of the Editor Board of the *International Journal of RF and Microwave Computer Aided Engineering* and the *Journal of Communications and Information Networks*. He was a recipient of the ISAP Young Scientist Travel Grant, Japan, in 2004. He was a co-recipient of the several best paper awards at international conferences. He received the Outstanding Reviewer Award from the IEEE MICROWAVE AND WIRELESS COMPONENTS LETTERS in 2010. He was a recipient of the General Assembly Young Scientists Award from the International Union of Radio Science in 2014 and the Hildegard Maier Research Fellowship of the Alexander Von Humboldt Foundation, Germany, in 2008. He was an Associate Editor of the *IEICE Transactions on Electronics* from 2010 to 2014 and a Guest Associate Editor of the Applied Computational Electromagnetics Society's Journal in 2017. He is an Associate Editor of the IEEE MICROWAVE AND WIRELESS COMPONENTS LETTERS.

Weng Cho Chew (S'79–M'80–SM'86–F'93) received the B.S., M.S., and Ph.D. degrees in electrical engineering, from the Massachusetts Institute of Technology, Cambridge, MA, USA, in 1976, 1978, and 1980, respectively.

From 1981 to 1985, he was a Program Leader and a Department Manager with the Schlumberger-Doll Research, Cambridge, MA, USA. He was the Director of the Electromagnetics Laboratory, University of Illinois at Urbana–Champaign (UIUC), from 1995 to 2007, where he was a Founder Professor of engineering from 2000 to 2005, a YT Lo Chair Professor from 2005 to 2009, and a Distinguished Ann and George Fisher Professor from 2013 to 2017. From 1985 to 2017, he was with UIUC, Champaign, IL, USA. From 2007 to 2001, he was the Dean of engineering with The University of Hong Kong, Hong Kong. In 2017, he joined Purdue University, West Lafayette, IN, USA, as a Distinguished Professor. He has both industry and academic experience. He has published over 1000 journals and conference papers, books, and lecture notes. His research group solved dense matrices for scattering problems with tens of millions of unknowns first time ever. He originated several fast algorithms for electromagnetics scattering and multiple-scattering inverse problems. His current research interests include wave physics, mathematics of inhomogeneous media, fast algorithms for scattering and radiation problems, and multiphysics phenomena, including quantum effects.

Dr. Chew is a fellow of the Optical Society of America, Institute of Physics, Electromagnetics Academy, and Hong Kong Institution of Engineers. He is a member of the U.S. National Academy of Engineering. He received the IEEE Graduate Teaching Award, the Electromagnetics Award, the CT Tai Distinguished Educator Award, best paper awards, IBM, and ACES CEM awards. He is the Editor-in-Chief of *Progress In Electromagnetics Research*. He is the President of the 2018 IEEE Antennas and Propagation Society. He is an ISI Highly Cited Author.